CHEMISTRY
A European Journal

A Journal of
ChemPubSoc Europe

Accepted Article

Title: Conversion from Heterometallic to Homometallic Metal-Organic Frameworks

Authors: Jeong Hwa Song, Giseong Lee, Jung Heum Yoon, Junyeon Jang, Doosan Choi, Heejun Yun, Kangin Kwon, Hojin Kim, Chang Seop Hong, Youngki Kim, Hogyu Han, Kwang Soo Lim, and Woo Ram Lee

To be cited as: *Chem. Eur. J.* 10.1002/chem.201904866

Link to VoR: http://dx.doi.org/10.1002/chem.201904866

Supported by
ACES

WILEY-VCH

10.1002/chem.201904866

WILEY-VCH

Conversion from Heterometallic to Homometallic Metal–Organic Frameworks

Jeong Hwa Song, [†,a] Giseong Lee, [†,b] Jung Heum Yoon,[a] Junyeon Jang,[a] Doosan Choi,[b] Heejun Yun,[d] Kangin Kwon,[b] Hojin Kim,[b] Chang Seop Hong,[b] Youngki Kim,[c] Hogyu Han,*[b] Kwang Soo Lim,*[c] and Woo Ram Lee*[a]

Abstract: Two new heterometallic metal–organic frameworks (MOFs), LnZnTPO **1** and **2**, and two homometallic MOFs, LnTPO **3** and **4** (Ln = Eu for **1** and **3**, and Tb for **2** and **4**; H_3TPO = tris-(4-carboxyphenyl)phosphine oxide) were synthesized, and their structures and properties were analyzed. They were prepared by solvothermal reaction of the C_3-symmetric ligand H_3TPO with the corresponding metal ion(s) (a mixture of Ln^{3+} and Zn^{2+} for **1** and **2**, and Ln^{3+} alone for **3** and **4**). Single-crystal X-ray diffraction (SXRD) analysis revealed that **1** and **3** are isostructural to **2** and **4**, respectively. Thermogravimetric analysis (TGA) showed that the framework is thermally stable up to about 400 °C for **1** and **2**, and about 450 °C for **3** and **4**. Powder X-ray diffraction (PXRD) analysis showed their pore structure changes during drying processes. The shapes of gas sorption isotherms for **1** and **3** are almost identical to those for **2** and **4**, respectively. Solvothermal immersion of **1** and **2** in Tb^{3+} and Eu^{3+} solutions resulted in the framework metal-ion exchange affording **4** and **3**, respectively, as confirmed by photoluminescence (PL), PXRD, infrared (IR), and inductively coupled plasma atomic emission spectroscopy (ICP-AES) analyses.

Introduction

Metal–organic frameworks (MOFs), also called porous coordination polymers (PCPs), are porous crystalline solids composed of metal nodes and organic bridges.[1] They are receiving much attention due to their ease of designed synthesis for implementing the predefined porosity and functionality in dimensional structures of porous materials. MOFs with predetermined structures and properties can be practically constructed by stitching metal-containing secondary building units (SBUs) formed *in situ* and organic linkers preassembled by organic synthesis. They are of great interest for gas storage,[2] gas capture and separation,[3] catalysis,[4] and sensing.[5]

Post-synthetic modifications of nanoporous MOFs can be an effective way to modulate their structures and properties. They include metal-ion exchange in the metal nodes and pores without losing the structural integrity of original MOFs.[6] While metal-ion exchange in the pores is frequently exercised, that in the metal nodes is rarely achieved due to its difficulty without significantly altering the original framework structure.[7] Accordingly, luminescent MOFs for sensing a specific metal ion or molecule are often designed based on their spectral changes upon exchange of metal ions and molecules in the pores, but rarely metal ions in the metal nodes.[8]

Lanthanide–organic frameworks (LOFs) containing lanthanide ions in the metal nodes can be useful for directly sensing metal-ion exchange in the metal nodes.[6d, 8d, 9] This is because the photoluminescence[10] (PL) intensity of LOFs decreases as the PL lanthanide ions in the metal nodes are removed from LOFs upon their exchange with other optically different metal ions. However, LOFs containing lanthanide ions in the metal nodes are rarely explored despite their potential for directly sensing metal-ion exchange in the metal nodes. LOFs with the open metal sites capable of increasing gas adsorption enthalpy for stronger metal ion–gas binding can be easily prepared.[9, 11] This is because lanthanide ions have high coordination numbers and thus lanthanide-coordinating solvent molecules can be easily removed under vacuum post-synthetically to form the open metal sites without losing the framework integrity of original LOFs. LOFs with the Lewis basic sites capable of increasing gas adsorption enthalpy can be prepared by using a phosphine oxide-based tricarboxylate ligand.[3c, 3e, 12] This is because this ligand has a lone pair of electrons on the O atom of the P=O bond, with the O atom arranged in the pores of LOFs. However, LOFs with open metal sites and Lewis basic sites[3c, 3e, 12c, 13] are rarely explored despite their potential for exhibiting improved gas capture properties.

Herein, we report the syntheses, structures, and properties of two new heterometallic MOFs, LnZnTPO **1** and **2**, and two homometallic MOFs, LnTPO **3**[9] and **4** (Ln = Eu for **1** and **3**, and Tb for **2** and **4**; H_3TPO = tris-(4-carboxyphenyl)phosphine oxide, Figure 1a). LnZnTPO and LnTPO containing both Ln^{3+} and Zn^{2+}, and Ln^{3+} alone, respectively, in the metal nodes were prepared by solvothermal reaction of the corresponding metal ion(s) with the C_3-symmetric ligand H_3TPO. The crystal structures,

[a] Prof. Dr. W. R. Lee, Dr. J. H. Song, J. H. Yoon, J. Jang, D. Choi, H. Yun
Department of Chemistry, Sejong University
05006, Seoul, Korea
E-mail: alchemist@sejong.ac.kr
[b] Prof. Dr. H. Han, Prof. Dr. C.S. Hong, G. Lee, K. Kwon, H. Kim
Department of Chemistry, Korea University
02841, Seoul, Korea
E-mail: hongyuhan@korea.ac.kr
[c] Dr. K. S. Lim
Korea Testing & Research Institute
13810, Gwacheon, Korea
[d] H. Yun
Program in Nano Science and Technology, Graduate School of Convergence Science and Technology, Seoul National University
08826, Seoul, Korea
[†] J.H.Song. and G.Lee. contributed equally to this work.

Supporting information for this article is available on the website at http://onlinelibrary.wiley.com

framework stabilities, and gas sorption properties of LnZnTPO and LnTPO were analyzed. Solvothermal immersion of LnZnTPO in Ln^{3+} solution resulted in metal-ion exchange in the metal nodes, affording LnTPO, as confirmed by spectroscopic analyses.

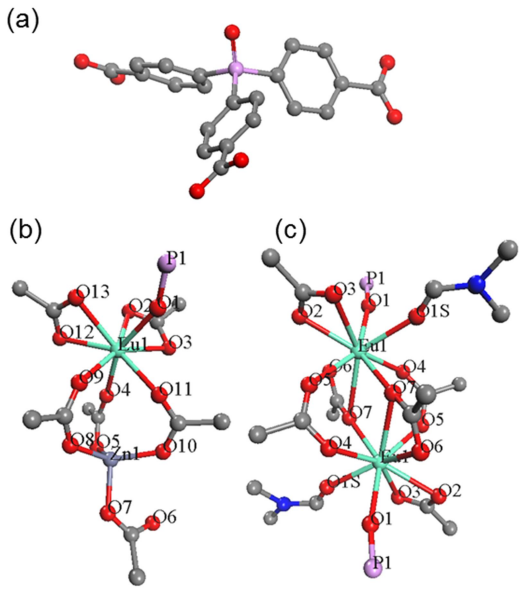

Figure 1. Structures of TPO ligand (a) and SBUs in **1** (b) and **3** (c). Structures of SBUs in **2** and **4** are shown in Figure S1 of the Supporting Information. The structure of TPO was modeled by single crystal X-ray diffraction analysis.

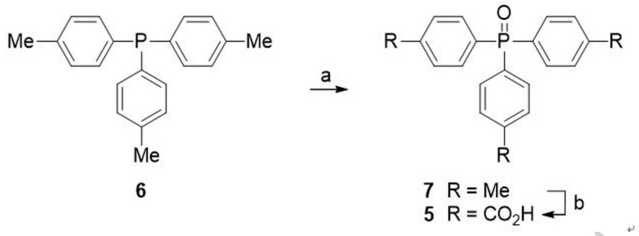

Scheme 1. [a]Reagents and conditions: (a) H_2O_2, CH_2Cl_2, rt, 100%; (b) $KMnO_4$, Py/H_2O (1:3), 140 °C, 84%.

Results and Discussion

Syntheses

Solvothermal reaction of H_3TPO with a mixture of $Ln(NO_3)_3{\cdot}6H_2O$ and $Zn(NO_3)_2{\cdot}6H_2O$ in DMF, or $Ln(NO_3)_3{\cdot}6H_2O$ alone in a mixed solvent (DMF/H_2O/MeOH = 3:3:1 v/v), together with a small amount of HNO_3, if needed, produced MOFs **1**–**4** as a colorless crystal. Here, H_3TPO **5** was synthesized from tri(*p*-tolyl)phosphine by the modified method of refs. 6a and 6c (Scheme 1). Oxidation of phosphorus to its oxide with H_2O_2 and then of the methyl to carboxyl group with $KMnO_4$ provides H_3TPO in a higher yield within a shorter time when compared to their oxidation only with $KMnO_4$. Note that acidic conditions are needed for the formation of **1**–**3** and adjusted with HNO_3.

Crystal structures

The single crystals of both **1** and **2** are in the triclinic system with a *P*-1 space group (Figure S1 and Tables S1 and S2 of the Supporting Information). They are isostructural, with the only difference being the Ln^{3+} ion (Eu^{3+} for **1** and Tb^{3+} for **2**), one of two different metal ions (Ln^{3+} and Zn^{2+}) present in their one SBU (Figure 1b and Figure S3 of the Supporting Information). The Ln^{3+} ion is coordinated by eight O atoms of five carboxylates and one P=O bond from six TPOs, whereas the Zn^{2+} ion is tetrahedrally coordinated by four O atoms of four carboxylates from four TPOs. These two different metal ions are triply bridged by three carboxylates of three TPOs, leading to the construction of a paddle wheel-like SBU acting as a 6-connected node. The average distance between Ln^{3+} and Zn^{2+} ions is 4.08 Å for **1** and 4.06 Å for **2**. The average Ln−O and Zn−O bond lengths are 2.46 Å and 1.95 Å for **1** and 2.44 Å and 1.94 Å for **2**, respectively. There are two kinds of TPOs in the unit cell, each of which has seven O atoms, six from three carboxylates and one from one P=O bond (Figure S1 of the Supporting Information). Only the six O atoms of one TPO are coordinated to metal ions in both kinds of TPOs, but show different coordination modes between the two kinds of TPOs. The O atom of the P=O bond, one of the seven O atoms presented in each TPO, is coordinated to the Ln^{3+} ion in one TPO centered at P1 atom and to neither Ln^{3+} nor Zn^{2+} ion in the other TPO centered at P2 atom. That is, the O atom of the P=O bond is coordinated to the Ln^{3+} ion and to none of the Ln^{3+} and Zn^{2+} ions when one and none of the six O atoms from three carboxylates is free from metal coordination, respectively. Note that the average Ln−O bond lengths are 2.385(3) and 2.404(3)−2.791(3) for a coordination bond of the Ln^{3+} ion with O atoms of the P=O bond and carboxylates, respectively, indicating a stronger 3D network-forming bond between the Ln^{3+} ion and the O atom of the P=O bond. In a unit cell of **1** and **2**, there are two SBUs, two Ln^{3+} ions, two Zn^{2+} ions, four TPOs, and four non-coordinated O atoms. SBUs are connected to each other by TPOs to form a three-dimensional structure and thereby a net entangled structure. Note that the frameworks of **1** and **2** have a charge of −1 per SBU when considering the charges of metal ions and ligand. One H_3O^+ ion per SBU was added when they were prepared by solvothermal reaction under acidic conditions as confirmed by elemental analysis.

The single crystals of both **3** and **4** are in the triclinic systems with a P-1 space group (Figure S2 and Tables S3 and S4 of the Supporting Information). They are isostructural, with the only difference being the Ln^{3+} ion (Eu^{3+} for **3** and Tb^{3+} for **4**), two of which are present in their one SBU (Figure 1c and Figure S4 of the Supporting Information). Each Ln^{3+} ion is coordinated by nine O atoms: eight O atoms of five carboxylates and one P=O bond from six TPOs and one O atom of one dimethylamide group from one DMF molecule. The two Ln^{3+} ions are quadruply bridged by four carboxylates of four TPOs, leading to the construction of a paddle-wheel like SBU acting as an 8-connected node. The average distance between two Ln^{3+} ions is 4.08 Å for **3** and 4.06 Å for **4**. The average Ln−O bond length is 2.34 Å for **3** and 2.31 Å for **4**. There are two TPOs in the unit cell

(Figure S2 of the Supporting Information). All seven atoms of each TPO are coordinated to the Ln^{3+} ion. The O atom of the P=O bond in each TPO centered at P1 atom is coordinated to each of two Ln^{3+} ions in one SBU. There are two kinds of carboxylates bridging between two Ln^{3+} ions. Two of those four carboxylates are bidentate, bridging two Ln^{3+} ions in such a way that each of two O atoms of one carboxylate is coordinated to each of two Ln^{3+} ions in one SBU. The two remaining carboxylates are tridentate, bridging two Ln^{3+} ions in such a way that one O atom of one carboxylate is coordinated to one of two Ln^{3+} ions and the other O atom to both of two Ln^{3+} ions. In a unit cell of **3** and **4**, there are one SBU, two Ln^{3+} ions, two TPOs, no non-coordinated O atoms, and two DMF molecules. SBUs are connected to each other by TPOs to form a three-dimensional structure and thereby a net entangled structure.

Solvent molecules in pores of **1**–**4** were removed using PLATON and Squeeze of WinGX. When solvent-accessible void volumes are calculated using the SOLV function of PLATON, **1**–**4** are 0.529, 0.562, 0.413, and 0.421 cm^3/g, which correspond to about 54.2%, 55.7%, 34.2%, and 49.2% of the total unit cell volume, respectively (Figure 2, Tables S5, and S6). Note that these values for **3** and **4** cannot be accurately calculated due to H_3O^+ ions in the pores.

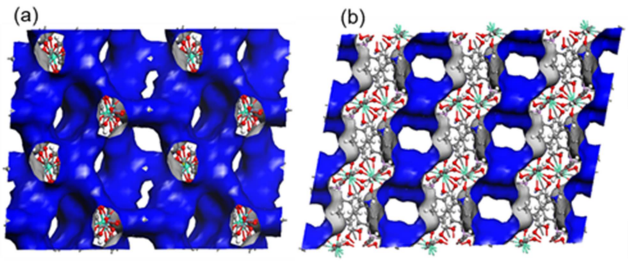

Figure 2. Solvent-accessible void volumes of **1** (a) and **3** (b). The results for **2** and **4** are almost identical to those for **1** and **3**, respectively.

Thermogravimetric and PXRD analysis

To investigate the gas adsorption properties of **1**–**4**, the structural stability of their pores in the empty state needs to be examined beforehand. TGA data show that **1** and **2** are thermally stable up to about 400 °C, whereas **3** and **4** are thermally stable up to about 450 °C (Figures S5 and S6 of the Supporting Information). The solvent molecules in the pore start to be removed at about 30 °C for **1**–**4**. The number of DMF and H_2O molecules in the pore is calculated by TGA to be 2.5 and 1.5 for **1**, 5.5 and 6 for **2**, 2 and 1.5 for **3**, and 2 and 2 for **4**. This is consistent with the number of solvent molecules identified by elemental analysis. The difference in the amount of solvent molecules in the pore between **1** and **2** and between **3** and **4** appears to be due to their different degrees of drying. Comparing the PXRD data of **1**–**4** prepared with and without complete removal of solvents in the pore shows that the peak shift occurs primarily at large angles upon their removal (Figure S7). This result indicates that the framework of **1**–**4** remains unchanged, but their pore structure is distorted and thus the structural environment in the pore changes during drying processes.[14] We performed Pawley refinement using experimental data and single crystal structure data through MS Modeling software. The simulated PXRD pattern data and the actual experimental data obtained through Pawley Refinement were displayed as one graph and inserted into the supporting information (Figure S8).

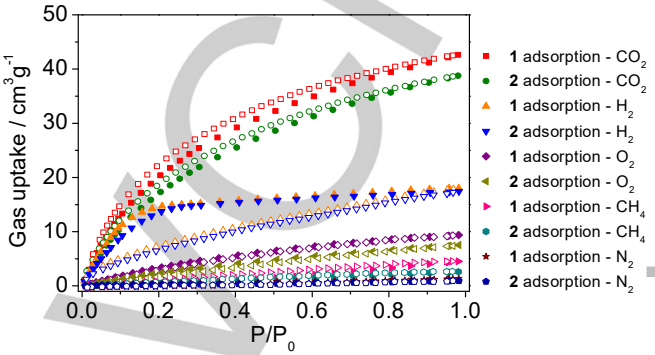

Figure 3. Gas sorption isotherms at 273 K for **1** and **2**. The solid and open shapes represent adsorption and desorption isotherms, respectively.

Gas sorption

To study the gas sorption properties of **1**–**4**, their gas sorption isotherms were measured at various temperatures (see the Supporting Information for full description). All the gas adsorption isotherms at 273 K for **1** and **2** are shown in Figure 3. The N_2 sorption isotherms at 77 K for **1** and **2** show typical type I behavior, thus ensuring permanent microporosity (Figure S9 of the Supporting Information).[15] Comparing the N_2 and H_2 adsorption isotherms at 77 K for **1** and **2**, it is seen that a large amount of N_2 is precipitously adsorbed even at low pressure. N_2 adsorption at 273 K for **1** and **2** was almost not achieved. The Brunauer–Emmett–Teller (BET) and Langmuir specific surface areas for **1** and **2** are shown in Table S5 of the Supporting Information. The pore volumes calculated from the single crystal structures of **1** and **2** are larger than those calculated from their experimental BET specific surface areas. This is due to the occupancy of pore space by H_3O^+ ions in **1** and **2**, both of which have an electric charge of −1 per SBU. The H_2 sorption isotherms at 77, 87, and 273 K for **1** and **2** show typical type I behavior (Figure S10 of the Supporting Information). The maximum adsorption amount of H_2 at 1 atm was measured for **1** and **2** at 77, 87, and 273 K. The maximum adsorption amount at theoretical high pressure was calculated using the Langmuir–Freundlich (LF) equation for **1** and **2** at 77 K (Figures S11 and S12 of the Supporting Information). The fitting parameters of the LF equation were determined for the H_2 adsorption isotherms at 77 K and 87 K and then plugged into the Clausius–Clapeyron equation to calculate H_2 adsorption enthalpy (Figures S11−S13 of the Supporting Information).[16] The maximum H_2 adsorption enthalpy is about 8.11 kJ/mol for **1** and about 7.63 kJ/mol for **2** (Figures S14 and S15 of the Supporting Information). Note that the O atom of the P=O bond in the TPO centered at P2 atom is arranged in the pores of **1** and **2**, acting as a Lewis basic site for strong interaction with H_2 molecules and thus increasing H_2 adsorption enthalpy. The average H_2 adsorption enthalpies were

7.69 and 6.64 kJ/mol for MOFs with and without open metal sites, respectively.[2a] Thus, the H_2 adsorption enthalpies for **1** and **2** having such Lewis basic sites are higher than those for MOFs having open metal sites. The CO_2 sorption isotherms at 195 and 273 K for **1** and **2** show typical type I behavior (Figure S16 of the Supporting Information). Their shapes at 195 K are similar to those of the N_2 sorption isotherms at 77 K. Compared with the N_2 adsorption isotherms, however, the CO_2 adsorption isotherms show a gentle curve, even with high adsorption achieved at 273 K. The O_2 sorption isotherms at 77 K for **1** and **2** show typical type I behavior at low pressure, but are attained only up to the relative pressure of 0.15, above which gaseous O_2 is driven to be liquefied by phase equilibrium (Figure S17 of the Supporting Information). The O_2 adsorption at 273 K is a very small amount compared with that at 77 K. The CH_4 sorption isotherms at 195 K for **1** and **2** show typical type I behavior (Figure S18 of the Supporting Information). Their shapes at 195 K are very similar to those of the H_2 sorption isotherms at 77 and 87 K. CH_4 adsorption at 273 K hardly occurs

The N_2 sorption isotherms at 77 K for **3** and **4** show typical type I behavior, as in the case of **1** and **2** (Figure S19 of the Supporting Information). Comparing the N_2 and H_2 adsorption isotherms at 77 K for **3** and **4**, it is seen that a large amount of N_2 is precipitously adsorbed at low pressure. The BET and Langmuir specific surface areas for **3** and **4** are shown in Table S6 of the Supporting Information. The pore volumes calculated from the single crystal structures of **3** and **4** are similar to those calculated from their experimental BET specific surface areas. The H_2 sorption isotherms at 77, 87, and 273 K for **3** and **4** show typical type I behavior, as in the case of **1** and **2** (Figure S20 of the Supporting Information). The maximum H_2 adsorption enthalpy is about 8.15 kJ/mol for **3** and about 7.62 kJ/mol for **4** (Figures S20−S24 of the Supporting Information). Note that each Ln^{3+} ion in **3** and **4** is coordinated by nine O atoms, one of which is from DMF molecule that can be removed upon high temperature activation under vacuum to form an open metal site without losing their framework integrity. Such an open metal site can act as a Lewis acidic site for strong interaction with H_2 molecules and thus increase H_2 adsorption enthalpy.[9] Thus, the H_2 adsorption enthalpies for **3** and **4** having such open metal sites are higher than those for MOFs having other open metal sites.[2a] The CO_2 sorption isotherms at 195 and 273 K for **3** and **4** show typical type I behavior, as in the case of **1** and **2** (Figure S25 of the Supporting Information).

Metal-Ion exchange

Since **1** and **2** contain photoluminescence (PL) Eu^{3+} and Tb^{3+} ions in the SBU, they can be a novel PL probe for directly sensing metal-ion exchange in the metal nodes. To test this possibility, the PL properties of **1** and **2** were investigated before and after they were subject to exchange of their Eu^{3+} and Tb^3 with Tb^{3+} and Eu^{3+}, respectively. The PL spectra of **1** and **2** dispersed in DMF at 1.0 mM are shown in Figure 4. Upon excitation of **1** at 275 nm, a total of five emission peaks associated with $^5D_0 \rightarrow {}^7F_J$ (J = 0–4) transitions appear, with the most intense peak for $^5D_0 \rightarrow {}^7F_2$ at 620 nm (red).[17] Upon excitation of **2** at 275 nm, a total of four emission peaks associated with $^5D_4 \rightarrow {}^7F_J$ (J = 3–6) transitions appear, with the most intense peak for $^5D_4 \rightarrow {}^7F_5$ at 550 nm (green).[17a, 18]

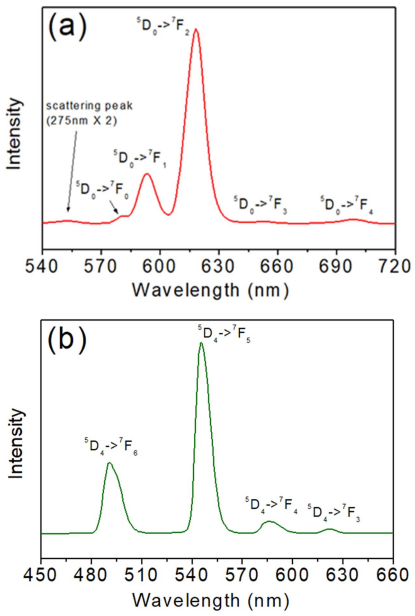

Figure 4. PL spectra of **1** (a) and **2** (b).

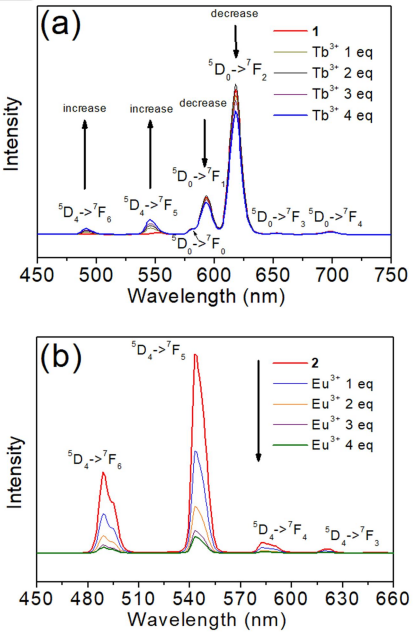

Figure 5. PL spectral changes of **1** (a) and **2** (b) in the presence of varying amounts (in equiv.) of Tb^{3+} and Eu^{3+} ions, respectively, at room temperature for 7 days.

The UV–vis spectra of TPO ligand show absorption peaks below 300 nm (Figure S26). The PL spectra of **1**–**4** upon excitation at 275 nm show metal-centered red (Eu) and green (Tb) emission peaks, respectively, which occur in LOFs through

the so-called antenna effect, without exhibiting ligand-centered emission peaks. This result indicates that the the efficient ligand to metal energy transfer occurs when **1**–**4** are excited at 275 nm. No overlap between absorption spectra of ligand and emission spectra of **1**–**4** indirectly indicates that ligand does not involve the emission (Figure S27 of the Supporting Information)

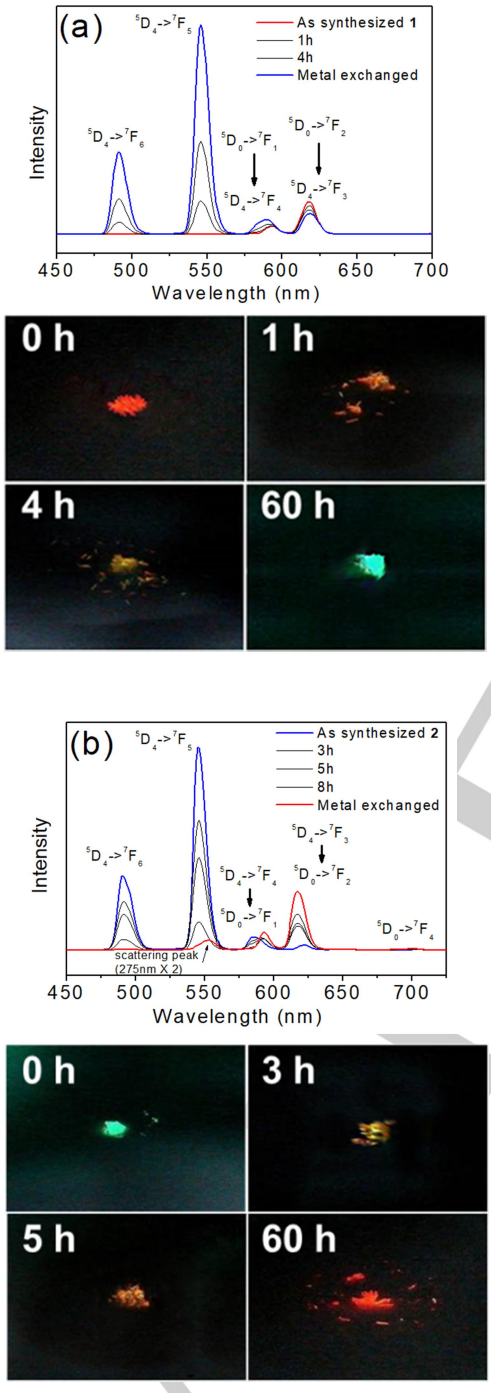

Figure 6. PL spectral changes of **1** (a) and **2** (b) in the presence of Tb^{3+} and Eu^{3+} ions, respectively, at 100 °C for varying times.

The PL spectra of **1** and **2**, which were dispersed in DMF at 1.0 mM and then placed in vials containing 0−4 equiv of Tb^{3+} and Eu^{3+} ions, respectively, at room temperature for 7 days, are shown in Figure 5. With an increasing amount of Tb^{3+} added to **1**, the PL intensity for $^5D_4 \rightarrow {}^7F_6$ and $^5D_4 \rightarrow {}^7F_5$, initially not detectable, increases, whereas that for $^5D_0 \rightarrow {}^7F_1$ and $^5D_0 \rightarrow {}^7F_2$ decreases. As the amount of Eu^{3+} added to **2** increases, the PL intensity of all peaks for $^5D_4 \rightarrow {}^7F_J$ (J = 3−6) decreases without new peaks appearing. The PL spectral changes were also investigated for various metal ions (nitrate as an anion) including other lanthanide ions and colorless transition metal ions (Figures S28-S46 of the Supporting Information). When they were added to **2**, however, no noticeably significant decrease in the PL intensity of **2** was observed, except for the Ce^{3+} ion. These results indicate that the metal-ion exchange in the metal nodes only occur for **2** in the presence of Ce^{3+} and Eu^{3+} ions. Note that the PL spectra of **3** and **4** are almost identical to those of **1** and **2**, respectively (Figures S47 and S48 of the Supporting Information). This phenomenon decreases the emission spectrum of Eu and Tb due to the slow exchange of ions at room temperature.

For rapid metal-ion exchange, experiments were conducted at high metal-ion concentrations and temperatures. The PL spectra of **1** and **2**, which were dispersed in DMF at 1.0 M, placed in vials containing 1.0 M Tb^{3+} and Eu^{3+} ions, respectively, at 100 °C for 0-60 h, and then diluted 1000-fold for PL measurement, are shown in Figure 6. Upon solvothermal immersion of **1** in Tb^{3+} solution, the peaks for $^5D_4 \rightarrow {}^7F_6$ and $^5D_4 \rightarrow {}^7F_5$, initially not shown, appear, and the peaks for $^5D_0 \rightarrow {}^7F_1$ and $^5D_0 \rightarrow {}^7F_2$ (red) apparently shift to those for $^5D_4 \rightarrow {}^7F_4$ and $^5D_4 \rightarrow {}^7F_3$ (green). These peak shifts arise from changes in the combined PL intensities for decreasing $^5D_0 \rightarrow {}^7F_1$ and $^5D_0 \rightarrow {}^7F_2$ and their overlapping but increasing $^5D_4 \rightarrow {}^7F_4$ and $^5D_4 \rightarrow {}^7F_3$ with increasing immersion time. The PL spectral change of **1** was completed within 8 h. The PL spectral change of **2** occurred in an opposite manner. Upon solvothermal immersion of **2** in Eu^{3+} solution, the peaks for $^5D_4 \rightarrow {}^7F_6$ and $^5D_4 \rightarrow {}^7F_5$ completely disappear, and the peaks for $^5D_4 \rightarrow {}^7F_4$ and $^5D_4 \rightarrow {}^7F_3$ (green) apparently shift to those for $^5D_0 \rightarrow {}^7F_1$ and $^5D_0 \rightarrow {}^7F_2$ (red). These peak shifts arise from changes in the combined PL intensities for decreasing $^5D_4 \rightarrow {}^7F_4$ and $^5D_4 \rightarrow {}^7F_3$ and their overlapping but increasing $^5D_0 \rightarrow {}^7F_1$ and $^5D_0 \rightarrow {}^7F_2$. The PL spectral change of **2** was completed within 12 h. As a result, the PL data show that Zn^{2+} and Eu^{3+} in **1** are replaced with Tb^{3+}, and Zn^{2+} and Tb^{3+} in **2** are replaced with Eu^{3+}. The color change shown in the photos of Figure 6 and displayed on the CIE 1931 chromaticities (Figure S49 of the Supporting Information) clearly shows that the metal ions were exchanged.[19]

The PXRD patterns of **1** and **2** before and after their solvothermal immersion in Tb^{3+} and Eu^{3+} solutions, respectively, are shown in Figure 7. The PXRD patterns of **1** and **2** substantially differ between before and after such solvothermal immersion. However, The PXRD patterns of **1** and **2** solvothermally immersed in Tb^{3+} and Eu^{3+} solutions are almost identical to those of **4** and **3** directly prepared by solvothermal reaction of H_3TPO with Tb^{3+} and Eu^{3+}, respectively. These results indicate that metal-ion exchange in the SBUs can occur

without their structural collapse under solvothermal conditions, converting **1** and **2** to **4** and **3**, respectively.

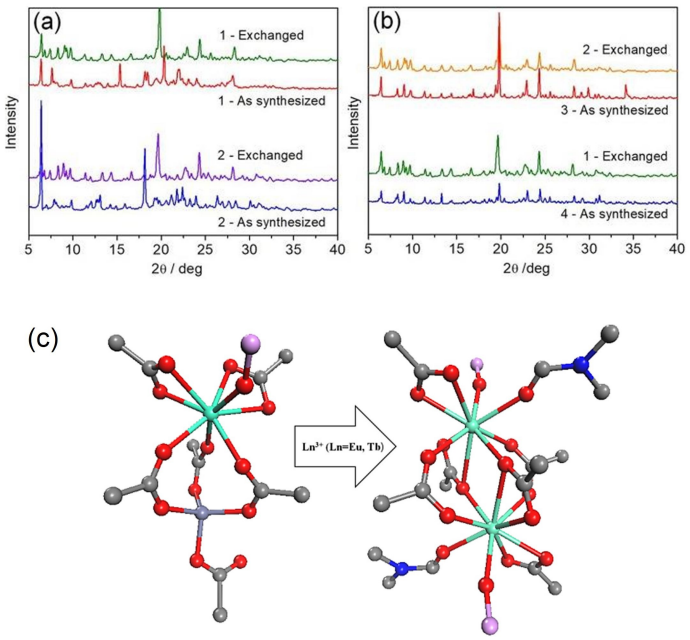

Figure 7. PXRD patterns of **1** and **2** before and after their solvothermal immersion in Tb^{3+} and Eu^{3+} solutions (a), and **3** and **4** directly prepared by solvothermal reaction of H_3TPO with Eu^{3+} and Tb^{3+} (b), and structural change in the SBUs upon metal-ion exchange converting **1** and **2** to **4** and **3** under solvothermal conditions (c), respectively.

The FTIR spectra of **1** and **2** before and after their solvothermal immersion in Tb^{3+} and Eu^{3+} solutions, respectively, are shown in Figure S50 of the Supporting Information. The FTIR spectra of **1** and **3** are nearly identical to those of **2** and **4**, indicating that the coordination modes between **1** and **2** and between **3** and **4** are almost vibrationally identical, as expected from having almost the same single crystal structures. The FTIR spectra of **1** and **2** differ between before and after such solvothermal immersion. Upon solvothermal immersion of **1** and **2**, the peak at 1616 cm^{-1} is split into several peaks, and the peaks at 1587, 1630, 1654, and 1664 cm^{-1} are shifted to 1178 cm^{-1} near 1163 cm^{-1} and to 1139 cm^{-1} near 1132 cm^{-1}. The FTIR spectra of **1** and **2** solvothermally immersed in Tb^{3+} and Eu^{3+} solutions are almost identical to those of **4** and **3** directly prepared by solvothermal reaction of H_3TPO with Tb^{3+} and Eu^{3+}, respectively. These results indicate that metal-ion exchange in the SBUs can occur without the collapse of the coordination modes under solvothermal conditions, converting **1** to 4 and **2** to **3**, respectively

The ICP-AES analyses of **1** and **2** before and after their solvothermal immersion in Tb^{3+} and Eu^{3+} solutions, respectively, are shown in Figure 8. Upon solvothermal immersion of **1**, the Eu^{3+} and Zn^{2+}-ion content in **1** decreases with a concomitant increase in its Tb^{3+}-ion content. Upon solvothermal immersion of **2**, the Tb^{3+} and Zn^{2+}-ion content in **2** decreases with a concomitant increase in its Eu^{3+}-ion content. The ICP-AES analyses showed that about 90% of metal-ion exchange was achieved within 60 h. That is, about 10% of the original metal ions remain and thus not all **1** and **2** have been converted to **4** and **3**, respectively. Note that only about 70% of Cu^{2+} ions are replaced with Zn^{2+} ions upon metal-ion exchange in CuHTPO.[6a] In **1**, Eu^{3+} and Zn^{2+} ions are diffused through the pores to the surface of EuZnTPO and then slowly replaced with Tb^{3+}. Since metal-ion exchange takes place first on the surface, TbTPO forms on top of EuZnTPO and completely surrounds EuZnTPO to form the core-shell like structure of EuZnTPO@TbTPO. Thereby, the inner Eu^{3+} and Zn^{2+} was isolated and could not be replaced with Tb^{3+} and thus only 90% of metal-ion exchange occurred.

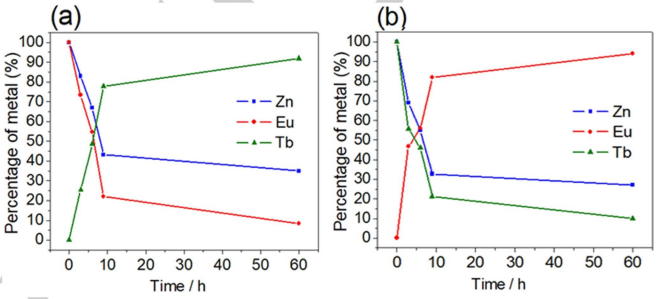

Figure 8. ICP-AES analyses of **1** (a) and **2** (b) before and after their solvothermal immersion in Tb^{3+} and Eu^{3+} solutions, respectively.

EDX elemental mapping of **1** and **2** after their solvothermal in Tb^{3+} and Eu^{3+} solutions, respectively, in Figure 51 of the Supporting Information. Upon solvothermal immersion of **1**, the small amount of Eu^{3+} and Zn^{2+} and the large amount of Tb^{3+} were observed. Likewise, upon solvothermal immersion of **1**, the small amount of Tb^{3+} and Zn^{2+} and the large amount of Eu^{3+} were observed.

Conclusions

In the present work, we prepared and characterized two new heterometallic MOFs, LnZnTPO, and two homometallic MOFs, LnTPO (Ln = Eu and Tb). Upon metal-ion exchange in the metal nodes under solvothermal conditions, LnZnTPO immersed in Ln^{3+} solution converts to LnTPO, as confirmed by spectroscopic analyses.

Experimental section

General. ^{1}H and ^{13}C spectra were recorded on a Bruker Ascend 500 NMR spectrometer. Chemical shifts (δ) and coupling constants (J) are reported in parts per million (ppm) and hertz (Hz), respectively. ^{1}H NMR spectra are referenced to DMSO-d_6 (0.03% v/v tetramethylsilane in DMSO-d_6) as an internal standard. ^{13}C NMR spectra are referenced to solvent (^{13}C: DMSO-d_6, δ 35.50 ppm) as an internal standard. High-resolution mass spectra (HRMS) were recorded on a JEOL JMS-700 mass spectrometer using a fast atom bombardment (FAB) technique. Thin-layer chromatography (TLC) was performed on silica gel 60 F_{254} precoated plates (0.25 mm thickness, Merck, Darmstadt). Flash

chromatography was carried out on silica gel 60 (230−400 mesh, Merck). Reagent-grade chemicals were purchased from Aldrich and TCI and used as received unless otherwise specified.

Thermogravimetric analyses were carried out at a ramp rate of 10 °C/min in a N_2 flow using a Scinco TGA N-1000 instrument. PXRD data were recorded using Cu Kα (λ = 1.5406 Å) on a Rigaku Ultima III diffractometer with a scan speed of 2°/min and a step size of 0.01°. Photoluminescence were measured with a Hitachi F-7000 FL spectrophotometer. The ICP data were collected on ICP-AES (ICP-OES; JY Ultima2C; Jobin Yvon, France) spectrometer. Infrared spectra were obtained from KBr pellets with a Nicolet-380 spectrometer (Thermo Electron Corp.). Gas sorption isotherms were measured using a BEL Belsorp mini II gas adsorption instrument up to 1 atm of gas pressure unless otherwise stated. The highly pure N_2 (99.999%), CO_2 (99.999%), H_2 (99.999%), CH_4 (99.999%), and O_2 (99.995%) were used in the sorption experiments. X-ray data for **3** was collected using synchrotron radiation (λ = 0.8000 Å) and a 2D-SMC ADSC Quantum-210 detector with a Pt-coated Si double crystal under a cooling stream of N_2 at the Pohang Accelerator Laboratory. The ADSC Quantum-210 ADX program was used for data collection and HKL3000 was used for cell refinement, data reduction, and absorption corrections. The structure was solved by direct methods and refined by the full-matrix least-squares method using anisotropic thermal parameters for non-hydrogen atoms with the SHELXTL program. X-ray data for **1, 2,** and **4** were collected on a Bruker SMART APEXII diffractometer equipped with graphite monochromated MoKα radiation (λ = 0.71073 Å). Preliminary orientation matrix and cell parameters were determined from three sets of ω scans at different starting angles. Data frames were obtained at scan intervals of 0.5° with an exposure time of 10 s per frame. The reflection data were corrected for Lorentz and polarization factors. Absorption corrections were carried out using SADABS. The structures of **1, 2,** and **4** were solved by direct methods and refined by full-matrix least-squares analysis using anisotropic thermal parameters for non-hydrogen atoms with the SHELXTL program. Guest molecules in **1**–**4** are significantly disordered and could not be modeled properly, thus the program SQUEEZE, a part of the PLATON package of crystallographic software, was used to calculate the solvent disorder area and remove its contribution to the overall intensity data.

Tri-*p*-tolylphosphine oxide (7). To a stirred solution of tri(*p*-tolyl)phosphine **6** (5 g, 16.43 mmol) in CH_2Cl_2 (100 mL) was added H_2O_2 (34.5%, 4.3 mL, 49.3 mmol). After stirring at rt for 10 min, the reaction mixture was quenched with H_2O (50 mL) and extracted with CH_2Cl_2 (50 mL × 2). The combined organic layers were dried over $MgSO_4$ and concentrated in vacuo to give **7** (5.25 g, 100%) as a white solid. TLC (MeOH/CH_2Cl_2 = 1:15) R_f = 0.51; ^{1}H NMR (500 MHz, DMSO-d_6) δ 7.46 (dd, J = 11.5, 8.0 Hz, 6H), 7.34 (dd, J = 8.0, 2.0 Hz, 6H), 2.36 (s, 9H); ^{13}C NMR (125 MHz, DMSO-d_6) δ 137.84 (d, J = 2.6 Hz), 127.43 (d, J = 9.9 Hz), 125.99 (d, J = 104.4 Hz), 125.20 (d, J = 12.7 Hz), 17.04; HRMS (FAB+) for $C_{21}H_{22}OP$ (MH^+), calcd 321.1408, found 321.1403.

H_3TPO ligand (5). To a refluxed and stirred solution of **7** (4 g, 3.12 mmol) in mixed solvent (pyridine/H2O = 1:3 v/v, 120 mL) were added $KMnO_4$ (23.7 g, 149.8 mmol). After stirring at 140 °C for 48 h, the reaction mixture was filtered through Celite 545. The filtrate was acidified with H_2SO_4 (20 mL) at 0 °C. The crude precipitate was filtered and recrystalized with cold MeOH (10 mL) to give **5** (4.3 g, 84%) as a white solid. TLC (MeOH/CH_2Cl_2 = 1:1) R_f = 0.23; ^{1}H NMR (500 MHz, DMSO-d_6) δ 13.40 (brs, 3H), 8.13 (dd, J = 8.5, 2.0 Hz, 6H), 7.82 (dd, J = 11.5, 8.0 Hz, 6H); ^{13}C NMR (125 MHz, DMSO-d_6) δ 162.57, 132.17 (d, J = 101.8 Hz), 130.29 (d, J = 2.8 Hz), 127.94 (d, J = 10.1 Hz), 125.59 (d, J = 11.8 Hz); HRMS (FAB+) for $C_{21}H_{16}O_7P$ (MH^+), calcd 411.0634, found 411.0630.

$(H_3O)[EuZn(TPO)_2](DMF)_x(H_2O)_y$ (1). A mixture of H_3TPO (100 mg, 0.244 mmol), $Eu(NO_3)_3{\cdot}6H_2O$ (42.76 mg, 0.096 mmol), $Zn(NO_3)_2{\cdot}6H_2O$ (42.84 mg, 0.144 mmol), and a small amount of HNO_3 in DMF (10 mL) was placed in a vial (10 mL) and heated at 100 °C for 72 h to reveal a needle-shaped colorless crystal (yield ≒ 40%). Anal. for $(H_3O)[EuZn(TPO)_2](DMF)_5(H_2O)_{3.5}$, calcd C 46.27, H 4.70, N 4.73, found C 46.21, H 4.45, N 4.65.

$(H_3O)[TbZn(TPO)_2](DMF)_x(H_2O)_y$ (2). A mixture of H_3TPO (100 mg, 0.244 mmol), $Tb(NO_3)_3{\cdot}6H_2O$ (42.50 mg, 0.096 mmol), $Zn(NO_3)_2{\cdot}6H_2O$ (42.84 mg, 0.144 mmol), and a small amount of HNO_3 in DMF (10 mL) was placed in a vial (10 mL) and heated at 100 °C for 72 h to reveal a needle-shaped colorless crystal (yield ≒ 60%). Anal. for $(H_3O)[TbZn(TPO)_2](DMF)_{5.5}(H_2O)_6$, calcd C 44.81, H 4.98, N 4.91, found C 44.85, H 4.85, N 5.12.

$[Eu(TPO)(DMF)](DMF)(H_2O)_x$ (3). A mixture of H_3TPO (100 mg, 0.24 mmol), $Eu(NO_3)_3{\cdot}6H_2O$ (104.40 mg, 0.24 mmol), and a small amount of HNO_3 in mixed solvent (DMF/H_2O/MeOH = 3:3:1 v/v, 10 mL) was placed in a vial (10 ml) and heated at 100 °C for 24 h to reveal an atypical-shaped colorless crystal (yield ≒ 60%). Anal. for $[Eu(TPO)(DMF)](DMF)(H_2O)_{1.5}$, calcd C 44.27, H 3.99, N 3.82, found C 44.56, H 3.79, N 3.49.

$[Tb(TPO)(DMF)](DMF)(H_2O)_x$ (4). A mixture of H_3TPO (100 mg, 0.24 mmol) and $Tb(NO_3)_3{\cdot}6H_2O$ (110.07 mg, 0.24 mmol) in mixed solvent (DMF/H_2O/MeOH = 3:3:1 v/v, 10 mL) was placed in a vial (10 mL) and heated at 70 °C for 24 h to reveal a small amount of a colorless crystal and a large amount of a bulk white crystalline powder (yield ≒ 80%). Anal. for $[Tb(TPO)(DMF)](DMF)(H_2O)$, calcd C 44.78, H 4.12, N 3.82, found C 44.40, H 3.86, N 3.84.

Acknowledgements

This work was supported by the National Research Foundation of Korea (NRF) grant funded by the Korean government (MSIP; Ministry of Science, ICT & Future Planning) (NRF-2017R1C1B5018060). This work was supported by a Korea University Grant. H.H. is grateful for the financial support from the National Research Foundation (NRF) of Korea funded by the Ministry of Science, ICT, and Future planning (NRF2019R1H1A2079948).

Keywords: Metal Organic Frameworks • Heterometallic Complexes • Conversion • Lanthanide metals • Photoluminesence

References

[1] a) H. Furukawa, K. E. Cordova, M. O'Keeffe, O. M. Yaghi, *Science* **2013**, *341*, 1230444; b) O. M. Yaghi, M. O'Keeffe, N. W. Ockwig, H. K. Chae, M. Eddaoudi, J. Kim, *Nature* **2003**, *423*, 705-714.

[2] a) J. Sculley, D. Yuan, H.-C. Zhou, *Energy Environ. Sci.* **2011**, *4*, 2721-2735; b) M. P. Suh, H. J. Park, T. K. Prasad, D. W. Lim, *Chem. Rev.* **2012**, *112*, 782-835; c) M. T. Kapelewski, T. Runčevski, J. D. Tarver, H. Z. H. Jiang, K. E. Hurst, P. A. Parilla, A. Ayala, T. Gennett, S. A. FitzGerald, C. M. Brown, J. R. Long, *Chem. Mater.* **2018**, *30*, 8179-8189; d) J. L. Rowsell, O. M. Yaghi, *Angew. Chem. Int. Ed.* **2005**, *44*, 4670-4679.

[3] a) S. Couck, J. F. M. Denayer, G. V. Baron, T. Remy, J. Gascon, F. Kapteijn, *J. Am. Chem. Soc.* **2009**, *131*, 6326-6327; b) A. Das, M.

Choucair, P. D. Southon, J. A. Mason, M. Zhao, C. J. Kepert, A. T. Harris, D. M. D'Alessandro, *Micropor. Mesopor. Mater.* **2013**, *174*, 74-80; c) T. M. McDonald, W. R. Lee, J. A. Mason, B. M. Wiers, C. S. Hong, J. R. Long, *J. Am. Chem. Soc.* **2012**, *134*, 7056-7065; d) K. Sumida, D. L. Rogow, J. A. Mason, T. M. McDonald, E. D. Bloch, Z. R. Herm, T. H. Bae, J. R. Long, *Chem. Rev.* **2012**, *112*, 724-781; e) W. R. Lee, S. Y. Hwang, D. W. Ryu, K. S. Lim, S. S. Han, D. Moon, J. Choi, C. S. Hong, *Energy Environ. Sci.* **2014**, *7*, 744-751; f) R. Haldar, S. K. Reddy, V. M. Suresh, S. Mohapatra, S. Balasubramanian, T. K. Maji, *Chem. Eur. J.* **2014**, *20*, 4347-4356; g) N. Planas, A. L. Dzubak, R. Poloni, L. C. Lin, A. McManus, T. M. McDonald, J. B. Neaton, J. R. Long, B. Smit, L. Gagliardi, *J. Am. Chem. Soc.* **2013**, *135*, 7402-7405; h) A. M. Fracaroli, H. Furukawa, M. Suzuki, M. Dodd, S. Okajima, F. Gandara, J. A. Reimer, O. M. Yaghi, *J. Am. Chem. Soc.* **2014**, *136*, 8863-8866; i) G. Chen, Z. Zhang, S. Xiang, B. Chen, *CrystEngComm* **2013**, *15*, 5232-5235; j) M. Y. Masoomi, K. C. Stylianou, A. Morsali, P. Retailleau, D. Maspoch, *Cryst. Growth Des.* **2014**, *14*, 2092-2096; k) S. Yang, J. Sun, A. J. Ramirez-Cuesta, S. K. Callear, W. I. F. David, D. P. Anderson, R. Newby, A. J. Blake, J. E. Parker, C. C. Tang, a. M. Schro¨der, *Nat. Chem.* **2012**, *4*, 887-894; l) P. Q. Liao, D. D. Zhou, A. X. Zhu, L. Jiang, R. B. Lin, J. P. Zhang, X. M. Chen, *J. Am. Chem. Soc.* **2012**, *134*, 17380-17383.

[4] a) A. Dhakshinamoorthy, Z. Li, H. Garcia, *Chem. Soc. Rev.* **2018**, *47*, 8134-8172; b) A. Taher, D. W. Kim, I.-M. Lee, *RSC Adv.* **2017**, *7*, 17806-17812; c) L. Zhu, X. Q. Liu, H. L. Jiang, L. B. Sun, *Chem. Rev.* **2017**, *117*, 8129-8176; d) A. Herbst, C. Janiak, *CrystEngComm* **2017**, *19*, 4092-4117; e) Y. B. Huang, J. Liang, X. S. Wang, R. Cao, *Chem. Soc. Rev.* **2017**, *46*, 126-157; f) Y. Z. Li, H. H. Wang, H. Y. Yang, L. Hou, Y. Y. Wang, Z. Zhu, *Chem. Eur. J.* **2018**, *24*, 865-871.

[5] a) F.-Y. Yi, D. Chen, M.-K. Wu, L. Han, H.-L. Jiang, *ChemPlusChem* **2016**, *81*, 675-690; b) A. Chidambaram, K. C. Stylianou, *Inorg. Chem. Front.* **2018**, *5*, 979-998; c) V. Chernikova, O. Yassine, O. Shekhah, M. Eddaoudi, Khaled N. Salama, *J. Mater. Chem. A* **2018**, *6*, 5550-5554; d) L. E. Kreno, K. Leong, O. K. Farha, M. Allendorf, R. P. Van Duyne, J. T. Hupp, *Chem. Rev.* **2012**, *112*, 1105-1125; e) X. Fang, B. Zong, S. Mao, *Nano-Micro Lett.* **2018**, *10*, 64.

[6] a) W. R. Lee, D. W. Ryu, W. J. Phang, J. H. Park, C. S. Hong, *Chem. Commun.* **2012**, *48*, 10847-10849; b) A. Nalaparaju, J. Jiang, *J. Phy. Chem. C* **2012**, *116*, 6925-6931; c) C. Zhao, X. Dai, T. Yao, W. Chen, X. Wang, J. Wang, J. Yang, S. Wei, Y. Wu, Y. Li, *J. Am. Chem. Soc.* **2017**, *139*, 8078-8081; d) S. Das, H. Kim, K. Kim, *J. Am. Chem. Soc.* **2009**, *131*, 3814–3815.

[7] Y. Noori, K. Akhbari, *RSC Adv.* **2017**, *7*, 1782-1808.

[8] a) Z. Jin, H. He, H. Zhao, T. Borjigin, F. Sun, D. Zhang, G. Zhu, *Dalton Trans.* **2013**, *42*, 13335-13338; b) J. Zhang, Y. Huang, D. Yue, Y. Cui, Y. Yang, G. Qian, *J. Mater. Chem. B* **2018**, *6*, 5174-5180; c) Y. Xiao, L. Wang, Y. Cui, B. Chen, F. Zapata, G. Qian, *J. Alloys Compd.* **2009**, *484*, 601-604; d) B. Zhao, H. L. Gao, X. Y. Chen, P. Cheng, W. Shi, D. Z. Liao, S. P. Yan, Z. H. Jiang, *Chem. Eur. J.* **2005**, *12*, 149-158; eS. Jensen, K. Tan, W. Lustig, D. Kilin, J. Li, Y. J. Chabal, T. Thonhauser, *J. Mater. Chem. C* **2019**, *7*, 2625-2632.

[9] W. R. Lee, D. W. Ryu, J. W. Lee, J. H. Yoon, E. K. Koh, C. S. Hong, *Inorg. Chem.* **2010**, *49*, 4723-4725.

[10] X.-Y. Li, W.-J. Shi, X.-Q. Wang, L.-N. Ma, L. Hou, Y.-Y. Wang, *Cryst. Growth Des.* **2017**, *17*, 4217-4224.

[11] a) S. R. Caskey, A. G. Wong-F, A. J. Matzger, *J. Am. Chem. Soc.* **2008**, *130*, 10870-10871; b) L. C. Lin, J. Kim, X. Kong, E. Scott, T. M. McDonald, J. R. Long, J. A. Reimer, B. Smit, *Angew. Chem. Int. Ed.* **2013**, *52*, 4410-4413; c) W. Lou, J. Yang, L. Li, J. Li, *J. Solid State Chem.* **2014**, *213*, 224-228.

[12] a) J. M. Gu, T. H. Kwon, J. H. Park, S. Huh, *Dalton Trans.* **2010**, *39*, 5608-5610; b) J. Qian, Q. Li, L. Liang, T. T. Li, Y. Hu, S. Huang, *Dalton Trans.* **2017**, *46*, 14102-14106; c) A. Demessence, D. M. D'Alessandro, M. L. Foo, J. R. Long, *J. Am. Chem. Soc.* **2009**, *131*, 8784-8786.

[13] X. Y. Li, Z. J. Li, Y. Z. Li, L. Hou, Z. Zhu, Y. Y. Wang, *Inorg. Chem.* **2018**, *57*, 12417-12423.

[14] a) R. Kitaura, K. Seki, G. Akiyama, S. Kitagawa, *Angew. Chem. Int. Ed.* **2003**, *42*, 428-431; b) I. Imaz, G. Bravic, J. P. Sutter, *Dalton Trans.* **2005**, 2681-2687.

[15] a) S. J. Gregg, L. S. W. Sing, *Adsorption, Surface Area, and Porosity*, **1984**; b) S. Brunauer, L. S. Deming, W. E. Deming, E. Teller, *J. Am. Chem. Soc.* **1940**, *62*, 1723-1732.

[16] J. Rouquerol, F. Rouquerol, P. Llewellyn, G. Maurin, K. Sing, *Adsorption by Powders and Porous Solids 2nd Edition*, **2013**.

[17] a) N. Sabbatini, M. Guardigli, J.-M. Lehn, *Coord. Chem. Rev.* **1993**, *123*, 201-228; b) D. Wang, C. Zheng, L. Fan, Y. Hu, J. Zheng, *Spectrochim Acta A Mol. Biomol. Spectrosc.* **2014**, *117*, 245-249.

[18] a) M. Khorasani-Motlagh, M. Noroozifar, S. Niroomand, A. Moodi, *J. Lumin.* **2013**, *143*, 56-62; b) T. Xia, T. Song, G. Zhang, Y. Cui, Y. Yang, Z. Wang, G. Qian, *Chem. Eur. J.* **2016**, *22*, 18429-18434.

[19] G. E. Gomez, A. M. Kaczmarek, R. Van Deun, E. V. Brusau, G. E. Narda, D. Vega, M. Iglesias, E. Gutierrez-Puebla, M. Á. Monge, *Eur. J. Inorg. Chem.* **2016**, *2016*, 1577-1588.

10.1002/chem.201904866

10.1002/chem.201904866

WILEY-VCH

Entry for the Table of Contents

FULL PAPER

Two new heterometallic metal-organic frameworks (MOFs), LnZnTPO **1** and **2**, and two homometallic MOFs, LnTPO **3** and **4** (Ln = Eu for **1** and **3**, and Tb for **2** and **4**; H_3TPO = tris-(4-carboxyphenyl)phosphine oxide) were synthesized, and their structures and properties were analyzed. Singe crystal X-ray diffraction (SXRD) analysis revealed that **1** and **3** are isostructural to **2** and **4**, respectively. Solvothermal immersion of **1** and **2** in Tb^{3+} and Eu^{3+} solutions resulted in the framework metal-ion exchange affording **4** and **3**, respectively, as confirmed by photoluminescence (PL), PXRD, infrared (IR), and inductively coupled plasma atomic emission spectroscopy (ICP-AES) analyses.

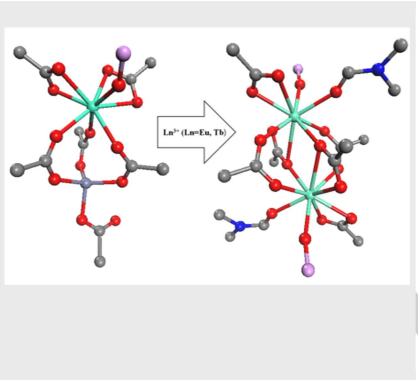

J. H. Song, G. Lee, J. H. Yoon, J. Jang, D. Choi, H. Yun, K. Kwon, H. Kim, C. S. Hong, Youngki Kim, H. Han, K. S. Lim,* and W. R. Lee**

Page No. – Page No.

Conversion from Heterometallic to Homometallic Metal-Organic Frameworks